J. Fluid Mech. (1998), *vol.* 357, *pp.* 351–379. Printed in the United Kingdom

Break-up and atomization of a round water jet by a high-speed annular air jet

By J. C. LASHERAS[1], E. VILLERMAUX[2] AND E. J. HOPFINGER[2]

[1] Department of Applied Mechanics and Engineering Sciences, University of California, San Diego, La Jolla, CA 92093-0411, USA

[2] LEGI-CNRS/UJF-INPG, BP 53, 38041 Grenoble Cedex, France

(Received 11 July 1996 and in revised form 16 October 1997)

The near- and far-field break-up and atomization of a water jet by a high-speed annular air jet are examined by means of high-speed flow visualizations and phase Doppler particle sizing techniques. Visualization of the jet's near field and measurements of the frequencies associated with the gas–liquid interfacial instabilities are used to study the underlying physical mechanisms involved in the primary break-up of the water jet. This process is shown to consist of the stripping of water sheets, or ligaments, which subsequently break into smaller lumps or drops. An entrainment model of the near-field stripping of the liquid is proposed, and shown to describe the measured liquid shedding frequencies. This simplified model explains qualitatively the dependence of the shedding frequency on the air/water momentum ratio in both initially laminar and turbulent water jets. The role of the secondary liquid break-up in the far-field atomization of the water jet is also investigated, and an attempt is made to apply the classical concepts of local isotropy to explain qualitatively the measurement of the far-field droplet size distribution and its dependence on the water to air mass and momentum ratios. Models accounting for the effect of the local turbulent dissipation rate in the gas on both the break-up and coalescence of the droplets are developed and compared with the measurements of the variation of the droplet size along the jet's centreline. The total flux of kinetic energy supplied by the gas per unit total mass of the spray jet was found to be the primary parameter determining the secondary break-up and coalescence of the droplets in the far field.

1. Introduction

The understanding of the break-up and atomization of liquid jets is fundamental to two-phase flow combustion and propulsion problems (Sutton 1992). In liquid propellant rocket engines, the reactants (fuel and oxidizer) are often supplied in an array of injectors where in each injector a jet of liquid oxygen is atomized by a high-speed annular hydrogen gas jet (Burick 1972). These types of atomizers when used in conventional air-supplied combustion applications are generically referred to as twin-fluid atomizers (Lefebvre 1989). Owing to the complexity of the underlying physical processes involved in the break-up of a liquid jet by a high-speed turbulent gas jet, this type of atomization is still poorly understood. Quantitative observations of the near field and measurements of the drop size and liquid void fraction are difficult to make, and often subject to large errors. Most of the past studies have focused on measuring the distribution of drop sizes at the spray's centreline at a certain fixed distance downstream of the nozzle ($x/D \geqslant 30$). From these point measurements, correlations

have been established for the drop size as a function of the flow parameters and the injector geometry (see for instance Lefebvre 1989; Gomi 1985). The dependence of the droplet size (typically characterized by the Sauter mean diameter defined by $D_{32} = \sum N_i d_i^3 / \sum N_i d_i^2$ where d_i is the diameter of each droplet, and N_i the number of droplets per unit volume in each size group) on the gas velocity has been found to be approximated by a power law $D_{32} \sim U_g^{-n}$ with n ranging usually from 0.8 to 1.3 (Ingebo 1991), possibly reaching a value as large as 2 in exceptional cases (Nukiyama & Tanasawa 1939; Gomi 1985). There is no convincing physical explanation for these power laws or even for why the drop size, in general, should follow a power-law dependence on the initial gas velocity. As high-speed photography and non-intrusive laser-based diagnostics have become more readily available, it is now possible to visualize the near field (Farago & Chigier 1992; Hopfinger & Lasheras 1994; Hardalupas & Whitelaw 1994; Englebert, Hardalupas & Whitelaw 1995) and to perform accurate measurements of the droplet size throughout the spray, thus opening new avenues in the development of theoretical models.

An early visual study of water jet instability, with or without coflowing or counterflowing air of velocity comparable to the liquid velocity, was performed by Hoyt & Taylor (1977). Their results indicate that in the near field the air stream has practically no influence on the instability which originates in the vorticity sheet of the water jet. Only further downstream, when perturbations are amplified, does the aerodynamic form drag on the liquid protrusions become active, and the air stream contributes to further destabilization of the water jet. This indicates that for the gas stream to affect the liquid jet instability appreciably in the near field, the gas momentum flux per unit volume has to be larger than or equal to the liquid momentum flux per unit volume. Surface tension is, of course, an important parameter and imposes a cut-off in the length scale of the amplified perturbations.

In the case of interest here, where a low-speed liquid jet is injected at the central axis of a high-speed coaxial air jet, the liquid break-up and droplet atomization can be divided into a near-field *primary break-up* region, and a far-field *secondary break-up* region. Both primary and secondary break-up have received considerable attention in the past. The primary break-up, which is dominant in the first few jet diameters, is essentially related to the non-miscible shear instability, and results in the stripping of the liquid jet by the high shear forces at the gas/liquid interface. Further downstream, droplet atomization may also occur from the deformation forces exerted on the droplets by the turbulent motion of surrounding air, a process known as *secondary atomization*.

Surface-tension-driven instability of liquid jets dates back to Rayleigh (1879), and Weber (1931) who included the effect of the viscosity of the liquid. These theories are relevant to ligament break-up in the near field (e.g. Lefebvre 1980). The destabilization of the liquid jet close to the nozzle exit is a Kelvin–Helmholtz type of instability where surface tension acts as a stabilizing force and imposes a lower cut-off for the waves which can grow (see Chandrasekhar 1961). This cut-off is given by a critical Weber number (Weber 1931; Chandrasekhar 1961). More specific theoretical models of the break-up of liquid sheets and jets in a gas stream have been developed subsequently (Mayer 1993; Dombrowski & Johns 1963; Adelberg 1968; and others). These models give correlations for the dependence of drop size on gas velocity and sheet thickness. Numerical simulations of two-dimensional interfacial instability by Mayer (1993), Keller *et al.* (1994) and Zaleski (1995) have also shown sheet formation and break-up, but these simulations are limited to low Reynolds number.

Individual liquid lumps stripped off from the central liquid core may still undergo

secondary break-up if the forces exerted by the turbulent air exceed the confinement due to the surface tension and the liquid viscosity. Fundamental studies of the break-up of individual drops submerged in turbulent flows were made by Kolmogorov (1949), Lane (1951), Hinze (1955), and many others. Three forces are involved in the splitting of the liquid, namely surface tension, viscous, and inertia forces. From dimensional arguments, Hinze showed that if τ is the force per unit area exerted by the gas on the surface of the droplet, the deformation process depends on two dimensionless groups, and a critical generalized Weber number, We_c', can then be defined as $We_c' = We_c[1+\Phi(N)]$, where $N = \mu/(\rho_l \sigma d)^{1/2}$ is a viscous group (or Ohnesorge number) which accounts for the viscosity of the liquid, and $We_c = \tau d/\sigma$ is the critical Weber number for the case of zero dispersed-phase viscosity.

Theoretical and experimental studies of single-drop shear break-up are numerous, and the reader is referred to Pilch & Erdman (1987) where the different scenarios depending on Weber number are discussed. When a water drop of size d is suddenly exposed to a uniform air flow of relative constant speed $(u_l - u_g)$ break-up will occur if the shear Weber number exceeds a critical value, $We_s = \rho_l(u_l-u_g)^2 d/\sigma > (We_s)_c$ (Hanson, Domich & Adam 1963). For a water droplet in air, Hinze (1955) showed that $(We_s)_c$ is of the order 10 (excluding here any resonant vibration or acceleration break-up). When the Reynolds number of the gas is very large, as it is in our application (i.e. of the order of 10^4 to 10^5), the motion of the gas is turbulent and the droplet may also break due to the dynamic pressure caused by the surrounding turbulence. A model for such a turbulence break-up was proposed by Kolmogorov (1949) and Hinze (1955). They defined a turbulent Weber number based on the difference in turbulent velocity on the scale equal to the drop size $We_t = \rho_g \overline{u(d)^2}\, d/\sigma$. Kolmogorov then postulated that when We_t is greater than a critical value, $(We_t)_c$, atomization of the liquid occurs as the dynamic pressure forces from the turbulent motion are sufficiently large to overcome the confinement of the surface tension. Hinze (1955) found that owing to resonant vibrations, the turbulent critical Weber number is typically smaller than 1, and he estimated a value of 0.59 from Clay's (1940) experiments.

In this paper we report an experimental study of the near- and far-field regions of the break-up of a round water jet by a high-speed annular air jet. Measurements of the frequency of the near-field interfacial instabilities are used to investigate the underlying physical mechanisms involved in the primary liquid break-up. The far-field secondary atomization is analysed by means of detailed measurements of both the droplet size and velocity distribution as well as turbulent characteristics of the atomizing air. In §2 we present the experimental set-up and procedures, and in §3 discuss the results of the near-field primary break-up. The primary break-up is first classified according to the water to air momentum ratio, the aerodynamic Weber number and the water and air Reynolds numbers. Measurements of the liquid shedding frequencies in each of the break-up modes are then presented, and a model of the near-field stripping is proposed. Finally, in §4 the role of the secondary break-up and quantitative relationships describing the influence of the turbulence on the break-up and coalescence of the drops is presented. Simplified models accounting for the local dissipation rate are then compared to the experimental evidence in §5.

2. Experimental conditions and procedures

The injector geometry is shown schematically in figure 1. The experiments are conducted at atmospheric pressure and water and air are used as working fluids. The jet nozzles are straight long tubes so that conditions at the outlet are a developed pipe

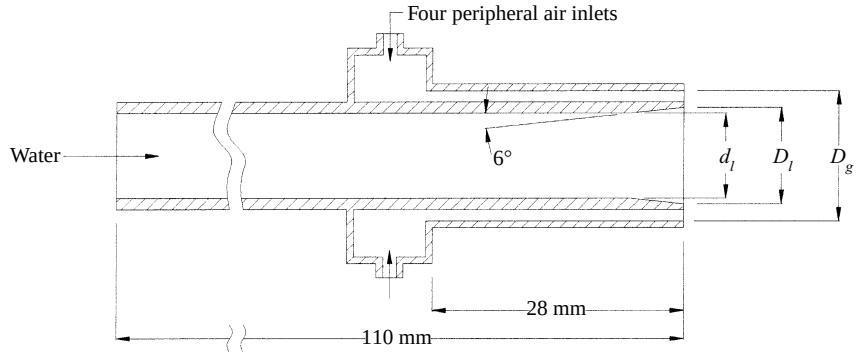

FIGURE 1. Coaxial jet nozzle configuration.

flow for the central water jet and a channel flow for the annular air jet. The inner tube is 110 mm long. It has an outer diameter of 4.2 mm and an inner diameter of $d_l = 2.9$ mm which is expanded through a 6° half cone angle to an outlet diameter $D_l = 3.8$ mm. This diffuser at the outlet modifies the pipe flow velocity profile somewhat, but it does not lead to flow separation in any of the experimental conditions reported here. The absence of separation was verified for the case of turbulent conditions at the exit of the water jet in a scale-up flow facility by Rehab, Villermaux & Hopfinger (1997). The nozzle diameters of the annular air jet are $D_g = 5.6$ mm and $d_g = 4.2$ mm, giving a gap spacing $h = 0.7$ mm over a length of 28 mm. The water nozzle velocity U_l was varied from 0.15 to 1.5 m s^{-1}, and the air velocity U_g from 20 to 250 m s^{-1}. These are section-averaged velocities, which are monitored with precision flow meters. The uniformity of the air flow at the nozzle's exit was checked with a total head tube of 0.7 mm outer diameter. In order to prevent any recirculation of the water spray in the test rig which could contaminate the measurements, we placed absorbing material in a receiving reservoir located far downstream ($x/D_g > 300$). Furthermore, extreme care was taken to prevent contamination from any possible recirculating flow by removing the spray reaching the damping reservoir with several suction fans.

Instantaneous photographs were taken with a CCD Sony video camera, with a framing rate 1/30 s and a shutter speed $\leqslant 10^{-4}$ s. Forward light scattering was used for these instantaneous images which have an average pixel resolution of about 20 μm. A high-speed video camera (Ektapro with a framing rate 1000 to 6000 frames/second) was also used to inspect the near-field break-up event and to measure the acceleration of the liquid by the air stream. The liquid shedding frequency was measured with a laser-photodiode arrangement placed one diameter downstream of the nozzles. This system consisted of a laser beam of 0.3 mm in diameter placed tangentially to the undisturbed water jet in the direction perpendicular to the jet's axis. As the interfacial instability developed, a photodiode recorded the attenuation signal produced as the interfacial waves attenuated the beam intensity. These waves are believed to be the precursors of the sheet/ligaments separating from the edge of the liquid jet. The attenuation signal from the photodiode was digitized at a rate of 10000 samples per second on a Le Croy 8212A A/D converter and subsequently processed in a frequency analyser.

The distribution of droplet size was measured with a phase Doppler particle sizer (PDPA) (Aerometrics Inc.). The jet was systematically measured at downstream locations in the range $90 \geqslant x/D_g \geqslant 7$. With a few exceptions, all the results reported here correspond to measurements performed at the jet's axis.

3. The near-field primary liquid break-up

3.1. *Flow parameters*

In jets, the most important parameter for the near-field development is the Reynolds number which has to be large ($Re \geqslant 10^3$) in order for the jet to become turbulent near its nozzle. For coaxial jets we can define a Reynolds number for the water jet, $Re_l = U_l D_l/\nu_l$, and a Reynolds number of the air jet, $Re_g = U_g D_g/\nu_g$. In addtion, we can define an effective Reynolds number to characterize the total flow (gas plus liquid) in the jet as

$$Re_{eff} = \left(\frac{U_g D_g}{\nu_g}\right)\left[\left(1-\frac{D_l^2}{D_g^2}\right)+\frac{D_l^2}{MD_g^2}\right], \tag{1}$$

where M is the momentum flux ratio per unit volume

$$M = \frac{\rho_g U_g^2}{\rho_l U_l^2}. \tag{2}$$

This quantity is an important parameter (Villermaux, Rehab & Hopfinger 1994) which was kept large in all the reported experiments. Other relevant parameters in the break-up and atomization process are the area (or diameter) ratio A_g/A_l, and the mass flux ratio

$$m = \frac{\rho_l U_l A_l}{\rho_g U_g A_g}. \tag{3}$$

The other useful non-dimensional number relevant to the liquid atomization is the initial aerodynamic. Weber number which is the ratio between the aerodynamic deformation pressure force exerted on the liquid (estimated with the initial velocity difference) and the restoring surface tension forces

$$We_0 = \frac{\rho_l(U_l-U_g)^2 D_l}{\sigma}, \tag{4}$$

where σ is the interfacial surface tension.

3.2. *Qualitative observations of the near-field primary atomization*

In figure 2 instantaneous images of the liquid jet break-up are presented for different flow conditions. In figure 2(*a–d*) the liquid velocity is $U_l = 0.33$ m s^{-1}, $Re_l = 1250$. The air velocity U_g is varied from 15.7 to 40.6 m s^{-1} corresponding to $850 \leqslant Re_g \leqslant 2100$. This condition corresponds to the initial aerodynamic Weber numbers $16 \leqslant We_0 \leqslant 110$, and $3 \leqslant M \leqslant 25$. Surface tension clearly dominates the near-field break-up in figure 2(*a–c*), but qualitatively seems to play a minor role in figure 2(*d*). Fibre-type ligaments begin to form in figure 2(*d*), and they are then observed to break into drops via a Rayleigh-type capillary break-up mechanism. Farago & Chigier (1992) report ligament formation when $We_0 \geqslant 100$. In figure 2(*e–h*) similar images are displayed but with the air velocity going up to 85 m s^{-1} ($Re_g = 4400$) and for a water velocity 0.58 m s^{-1} ($Re_l = 2230$). For the geometry investigated in the present experiments (the diameter of the liquid jet is larger than in the experiments of Farago & Chigier), fibre-type ligaments are seen more clearly when $We_0 \geqslant 200$ (figure 2*g*). These fibres are also seen to decrease in size as the Weber number is increased. However, increasing the air velocity for a given water velocity increases not only the Weber number but also the

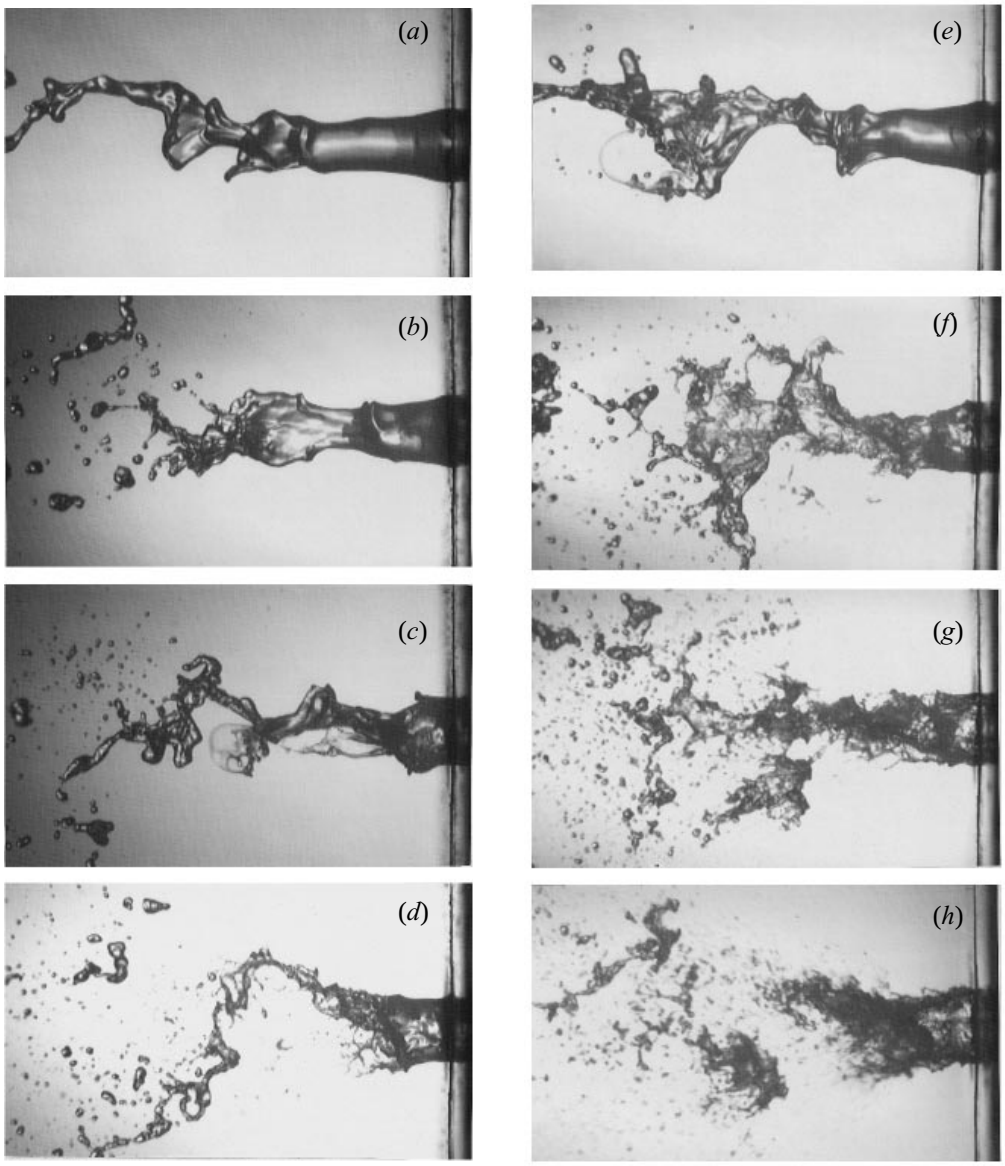

FIGURE 2. Instantaneous flow visualization of the break-up of the liquid jet by the annular air jet. (*a*) $U_g = 15.75$ m s^{-1}, $M = 3.8$, $We_0 = 16$, $Re_l = 830$; (*b*) $U_g = 21.7$ m s^{-1}, $M = 7.35$, $We_0 = 31$, $Re_l = 1120$; (*c*) $U_g = 28$ m s^{-1}, $M = 12.2$, $We_0 = 52$, $Re_l = 1450$; (*d*) $U_g = 40.6$ m s^{-1}, $M = 25$, $W_0 = 110$, $Re_l = 2100$; (*e*) $U_g = 21.7$ m s^{-1}, $M = 2.05$, $We_0 = 31$, $Re_l = 1120$; (*f*) $U_g = 40.6$ m s^{-1}, $M = 7.0$, $We_0 = 110$, $Re_l = 2100$; (*g*) $U_g = 56$ m s^{-1}, $M = 13$, $We_0 = 210$, $Re_l = 2900$; (*h*) $U_g = 85.4$ m s^{-1}, $M = 31$, $We_0 = 489$, $Re_l = 4420$.

momentum flux ratio M. In figure 3(*a–c*) we show images for different Weber numbers and also for the same Weber number but different values of M (compare figures 3*a* and 3*b*). The ligament size in the near field seems similar in the two images 3(*a*) and 3(*b*), but at the lower M an intact liquid core persists further downstream. When the Weber number is large, the momentum flux ratio is, therefore, the crucial parameter in determining the liquid core length (or liquid intact length).

The other point of interest in these flow visualizations is the strong spiral mode and

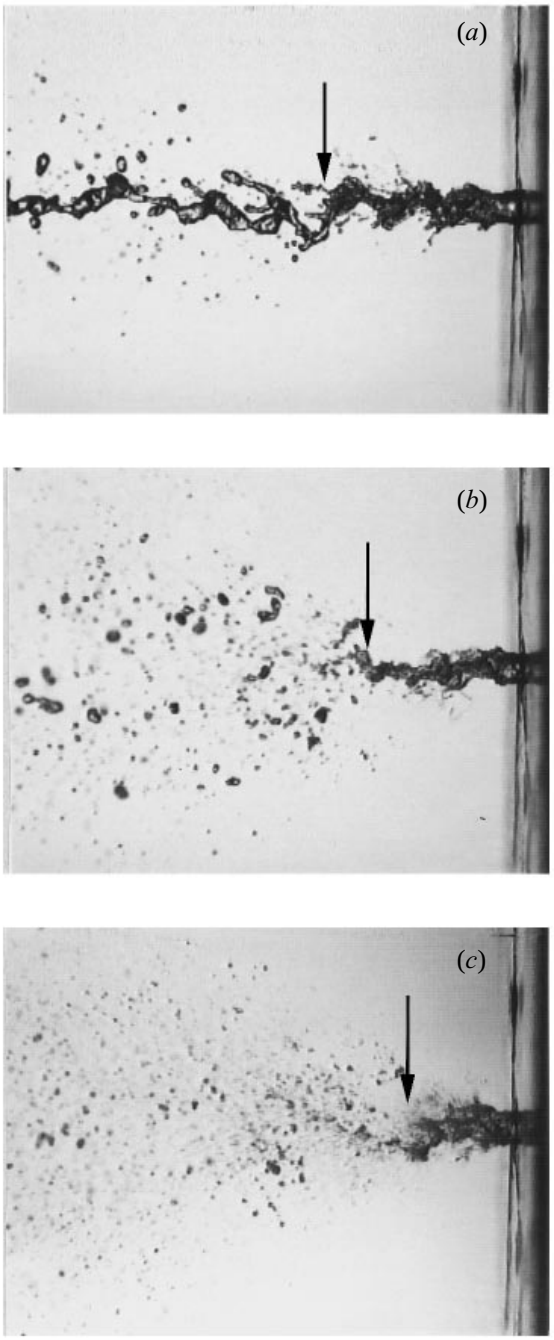

FIGURE 3. Instantaneous flow visualization of the jet break-up. (*a*) $U_l = 1.0$ m s^{-1}, $M = 2.5$, $We_0 = 200$; (*b*) $U_l = 0.5$ m s^{-1}, $M = 10$, $We_0 = 200$; (*c*) $U_l = 0.5$ m s^{-1}, $M = 40$, $We_0 = 800$.

the acceleration of the liquid sheet, particularly visible at the lower values of We_0 (figures 2*b* and 2*e*). Furthermore, figure 2(*b*) seems to suggest that although the final liquid atomization is a chaotic process (Hardalupas & Whitelaw 1994; Engelbert *et al.* 1995) the water is peeled off from the jet's surface at nearly constant frequencies, an

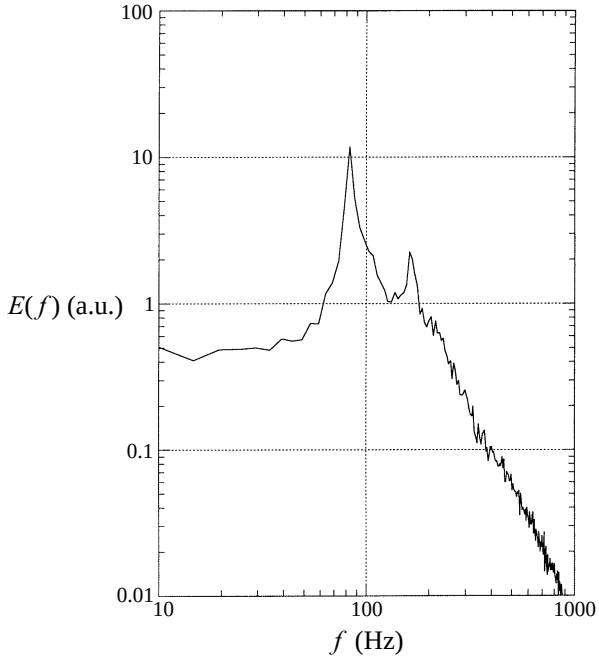

FIGURE 4. Power spectrum of the photodiode signal indicating the liquid shedding frequency. $U_l = 0.3$ m s^{-1} and $U_g = 25$ m s^{-1}.

important point which was corroborated by the high-speed films and by local laser attenuation measurements discussed in §3.3. It should also be noticed that for the mass flux ratios shown in figures 2 and 3 ($m > 5$) there are always relatively large lumps of liquid still present far downstream. These lumps are seen to become smaller and fewer in number at the larger momentum flux ratios and smaller mass flux ratios.

3.3. *Liquid shedding frequency*

At the air–water interface, the shear stresses are continuous. At large values of M, the interfacial water layer is accelerated by the air to a velocity U_i larger than U_l. The case of interest here is a turbulent air stream ($Re_g \geqslant 1000$) with either a turbulent or a laminar water jet (Re_l respectively larger or smaller than about 2000). In both cases, and in the limit of large momentum ratio M, the interfacial velocity should be proportional to $(\rho_g/\rho_l)^{1/2}\, U_g$.

In the case of turbulent air and laminar water, the interfacial velocity is estimated by equating the shear stresses at the interface. Indeed, the acceleration of the liquid at the interfaces induces, by diffusion of vorticity, a velocity profile in the liquid whose thickness $\delta(x)$ increases with the downstream distance x from the nozzle exit. Assuming, for clarity of the argument $U_i \gg U_l$ (this condition might, however, not always be fulfilled, see Dimotakis 1986 and Raynald 1997), continuity of stress results in

$$\mu_l \frac{U_i}{\delta} \approx \rho_g\, u^{*2}, \tag{5}$$

where $\frac{1}{2} C_g\, U_g^2 = u^{*2}$, $C_g = 5 \times 10^{-3}$ being a friction coefficient (Schlichting 1987). The liquid boundary layer thickness $\delta(x)$ grows until it ultimately reaches a value δ_c such that the Reynolds number based on U_i and δ_c, $Re_c = U_i\, \delta_c/\nu_l$, is large enough to allow

the instability of the shear layer. At that critical location $x_c \approx \nu_l/U_i$, one has

$$U_i \approx (Re_c\, C_g \rho_g/\rho_l)^{1/2}\, U_g. \tag{6}$$

However, when both the liquid and the gas are turbulent at the nozzle exit, the condition of continuity of the stress at the interface becomes

$$\rho_l\, U_l^2 \approx \rho_g\, u^{*2}, \tag{7}$$

leading to the same scaling dependency as shown in (6).

The wavelength, λ, of the Kelvin–Helmholtz instability of the shear layer developing between a light stream and a slower dense stream is proportional to the initial thickness of the velocity profile, δ_0, and to the square root of the density ratio, i.e. $\lambda \approx \delta_0(\rho_l/\rho_g)^{1/2}$ (Raynald *et al*. 1997). Thus, the shedding frequency $f \approx U_i/\lambda$ can be written in all cases as

$$f \approx \frac{\rho_g}{\rho_l}\frac{U_g}{\delta_0}. \tag{8}$$

Different dependencies of the frequency f on the gas velocity U_g can exist depending on the mechanism which sets the thickness δ_0. Two extreme cases can be expected. When the liquid is laminar and the gas has a fully developed turbulent profile at the nozzle exit, the length scale becomes the viscous sublayer, ν_g/u^*, as has been shown recently measurements by Raynald (Raynald, Villermaux & Hopfinger 1998). In this case

$$f \approx \frac{\rho_g}{\rho_l}\frac{C_g^{1/2}}{\nu_g}\, U_g^2. \tag{9}$$

If both the liquid and the gas are turbulent, the maximal scale of the disturbances is fixed by the thickness of the gap, $D_g - D_l$. Therefore, the shedding frequency becomes

$$f \approx \frac{\rho_g}{\rho_l}\frac{U_g}{D_g - D_l}. \tag{10}$$

If, on the other hand, the gas stream is laminar and the exit vorticity thickness has a boundary layer dependency on the gap Reynolds number $\rho_0/(D_g - D_l) \approx Re_g^{-1/2}$, an intermediate effect of f on U_g between the limits described by equations (9) and (10) should be expected.

The frequencies determined from the spectrum of the photodiode signal (an example of which is shown in figure 4) as a function of U_g, for different values of U_l, are shown in figure 5(*a*). It is seen that the observed trends correlate well with equation (9) when the water velocity $U_l < 0.5\ \mathrm{m\ s^{-1}}$ ($Re_l < 2\times10^3$), and with equation (10) when $U_l > 0.5\ \mathrm{m\ s^{-1}}$ ($Re_l > 2\times10^3$), and $200 > We_0 > 100$.

When the momentum ratio is large $M \geqslant M_c$ (see below for a definition of M_c) a recirculating air cavity exists on the jet's centreline which oscillates at a lower frequency, f_r, and this frequency coexists with the shear instability frequency. The origin and the features of this low-frequency oscillation (often referred to as a 'superpulsating mode') are explained in Villermaux & Hopfinger (1994*a*, *b*). Their study emphasized the role of the recirculation on the origin of this slow mode which is distinct from the primary shear instability and can be modelled by an amplitude equation with time delay (see also Villermaux *et al*. 1994 and Rehab *et al*. 1997).

3.4. *Liquid intact length*

For zero liquid mass flow a separated flow region replaces the liquid cone. By traversing a small total head tube (0.7 mm outer and 0.4 mm inner diameter) downstream, starting at the nozzle, it was found that the pressure changed from a

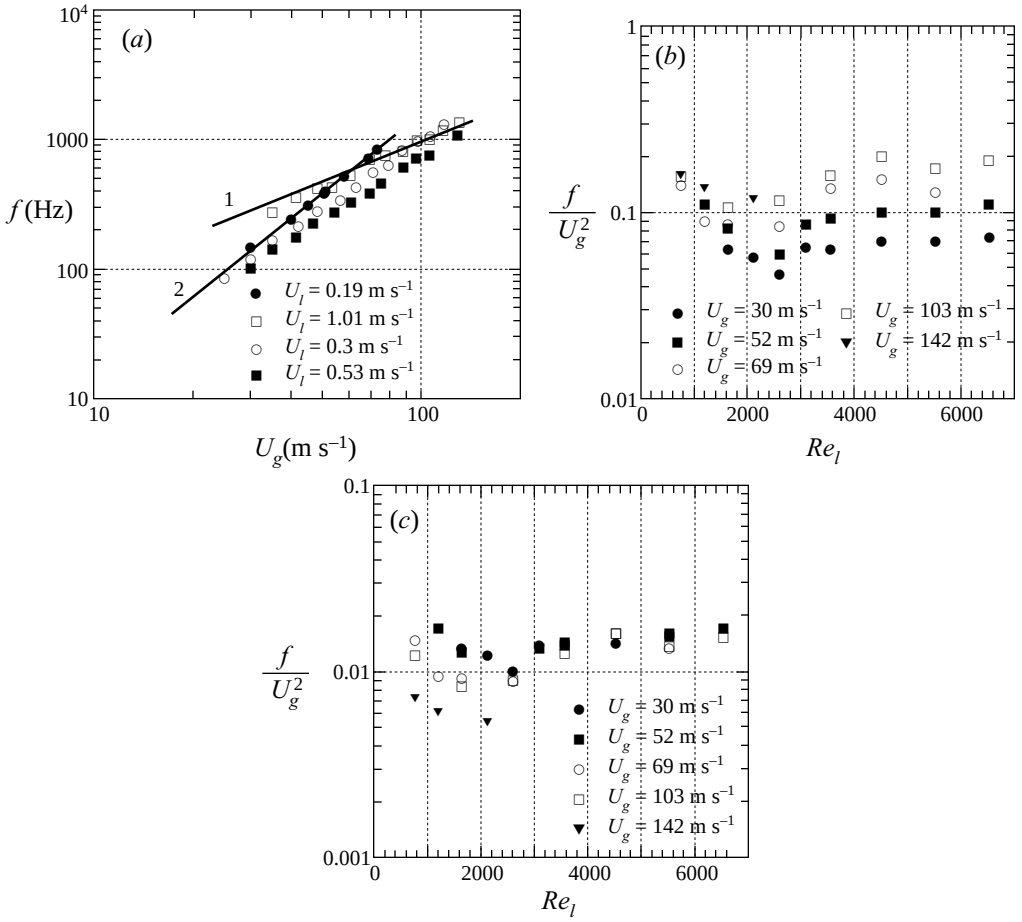

FIGURE 5. (*a*) Liquid shedding frequency as a function of the air velocity for different water velocities. (*b*) Liquid shedding frequencies rescaled with equation (10) versus the liquid Reynolds number for several gas velocities. In the limit of a very small liquid Reynolds number, the shedding frequency is independent of the liquid velocity and is proportional to the square of the gas velocity. (*c*) Liquid shedding frequencies rescaled with equation (11) versus the liquid Reynolds number for several gas velocities. When the liquid is turbulent (Reynolds number > 2000) the shedding frequency is linearly proportional to the gas velocity.

negative value at the nozzle exit to the ambient pressure at a downstream distance $L_0 = 0.8D_l$, and reached a maximum at a location of $1.5D_l$. The length of zero Δp corresponds to the length of a separated flow cavity, the equivalent of the separated flow region behind a backward-facing step. Note, that the axisymmetric flow cavity is, however, much shorter than the two-dimensional flow cavity. The maximum pressure corresponds to the location where the annular jet has merged into an axisymmetric jet flow.

When water is supplied at the centre, the recirculation of air may still occur when the water flow rate is less than the rate at which water can be entrained by the air stream over the distance L_c, where L_c is the critical length for which the water just fills the cavity. L_c will be of the order of, but larger than, L_0 because the pressure defect at the centre is less when there is water supplied (less convergence of the streamlines). The momentum flux ratio corresponding to L_c is the critical value M_c. Taking L_c as a reference length, we have for momentum flux ratios $M < M_c$ a liquid break-up

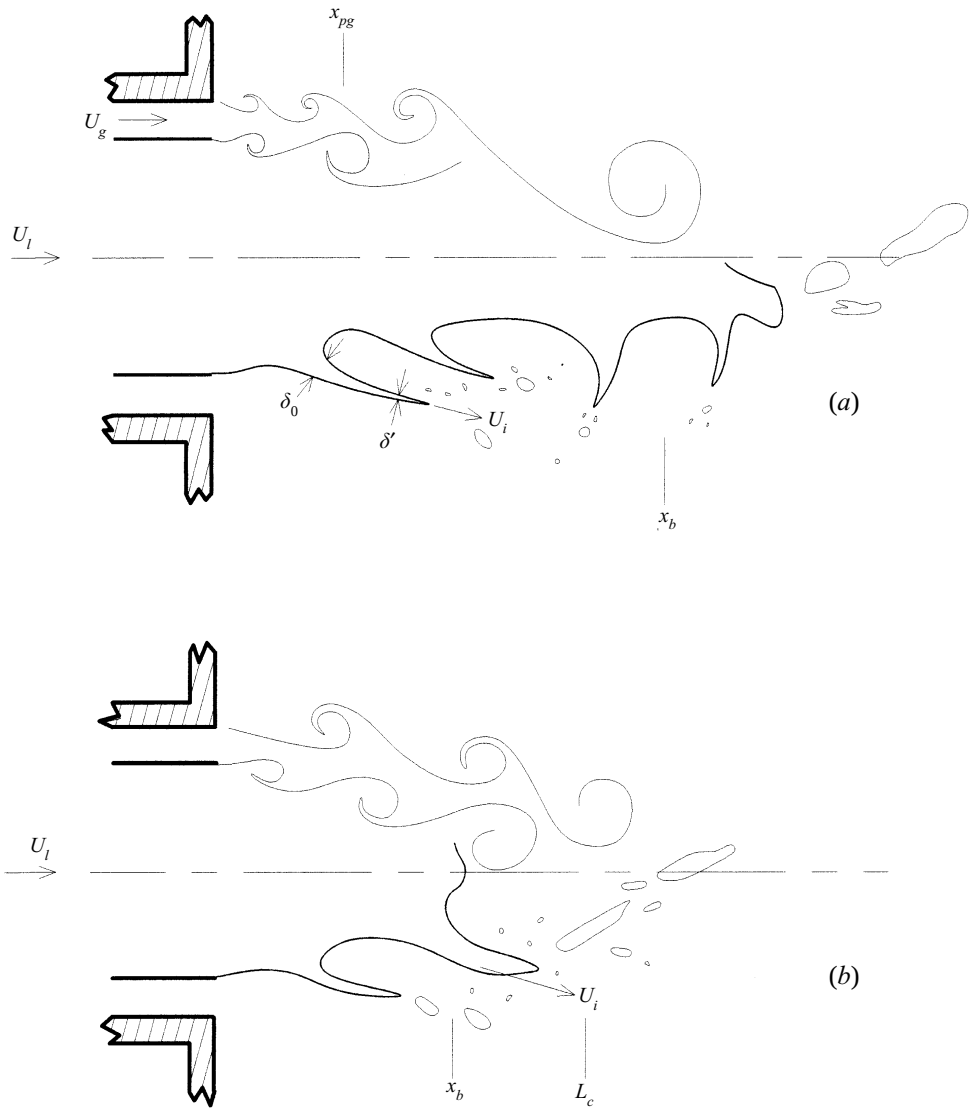

FIGURE 6. Schematic view of the liquid break-up. x_b = liquid break-up length or liquid intact length. U_i = velocity of the liquid/air interface, δ_0 = characteristic thickness of the liquid sheets. (*a*) $x_b > L_c$, (*b*) $x_b < L_c$.

length $x_b > L_c$ (figure 6*a*), whereas when $M > M_c$, the liquid cone is chopped off and $x_b < L_c$ as sketched in figure 6(*b*).

A simple entrainment model can account for this observed behaviour. When the air momentum is dominant, the liquid ligaments are entrained into the air stream. The local pressure drop in the air stream due to the turbulent motions of r.m.s. velocity u'_g is proportional to $\rho_g u'^2_g$. This will cause an entrainment of water into the air stream at a velocity u_e given by the relation

$$\rho_l u_e^2 = C_e \rho_g u'^2_g, \tag{11}$$

where C_e is a factor which can be determined from experiments with jets in equal-density fluids. This relation is valid when both the air Reynolds number and the initial

aerodynamic Weber number are sufficiently large for the entrainment not to be limited by surface tension. As mentioned above, according to figures 2 and 3, the break-up can be considered as independent of, or weakly dependent on, surface tension when $We_0 > 200$. When taking a critical value of 10 for the local shear Weber number, the scales affected by surface tension are then less than $D_l/20 = 150$ μm. Assuming that the entrainment velocity remains constant with the downstream distance, conservation of liquid mass requires that $u_e A = U_l \pi D_l^2/4$, where A is the surface area of the interface (Villermaux 1995). For the geometry of our injectors the air potential cone length $x_{pg} \approx 5h \leqslant D_l$, so that when $x_b = D_l$ the turbulence responsible for the entrainment is $u_g' = \alpha(U_g - U_l)$, and when x_b is considerably longer than D_l, $u_g' = \alpha U_g$. For the particular case of water–air, $U_l \ll U_g$ and the two expressions are nearly identical. Thus, taking $u_g' = \alpha U_g$, and approximating the surface of the interface as a cone,

$$\frac{x_b}{D_l} = \left(\frac{\rho_l U_l^2}{4C_e \rho_g \alpha^2 U_g^2} - \frac{1}{4}\right)^{1/2}. \tag{12}$$

Using $\alpha = 0.17$, $C_e = 0.25$ (estimated from the length of the potential cone in a single-phase jet), and neglecting the 1/4 in (12), the break-up length is

$$\frac{x_b}{D_l} = \frac{1}{\alpha M^{1/2}} \approx \frac{6}{M^{1/2}}. \tag{13}$$

For coaxial jets of equal density the inner jet cone length is given by equation (13) (Rehab *et al.* 1997). In water–air coaxial jets, the water cone length also depends weakly on the water velocity for a given M (Raynald *et al.* 1997).

The length given by equation (13) is indicated in the photographs of figures 2 and 3. Although these images do not allow testing of the validity of equation (13), the observed trends are consistent. The existence of oscillations in the liquid cone length is related to the spiral mode instability, and the periodic shedding of water makes the determination of the intact length from instantaneous photographs difficult. For instance, Eroglu, Chigier & Farago (1991) determined the intact length from four to seven photographs taken for the same flow conditions. In their experiments, the initial Weber number was less than 250 and, therefore, in most of their experiments the intact length depends also on the Weber number. However, it is surprising to note that in the past the momentum flux ratio has not been considered as the determining parameter of the liquid intact length, not even when the initial Weber number is very large.

It should be noted that the liquid intact length defined by equation (13) corresponds to the distance from the water jet nozzle to where the liquid fraction on the jet axis is close to 1. Thus, it has some correspondence to the potential cone region in a single-phase jet. It is also possible to define the liquid cone length by the distance from the nozzle at which the void fraction is a given value, say 0.5 (as has been used in other investigations).

The mass flux ratio is a quantity which should appear in the expression for the intact length (equation (14)). In deriving this equation, it has been assumed that over the distance x_b the air velocity remains nearly constant. The two annular shear layers merge downstream of $x_{pg} \approx D_l$ and form a nearly two-dimensional jet. This jet velocity may decrease more rapidly than in a usual two-dimensional jet because momentum has to be transferred to the entrained liquid. However, a model taking into account the effect of the liquid mass flux could not be verified by the present experiments. The important point to be made here is that for high initial Weber number and high gas

Reynolds number, as is generally the case in liquid propellant rocket engine applications, the momentum flux ratio M is the dominant parameter. Equation (13) provides a physical explanation for this being the case.

From equation (13) we can determine the critical value of M at which the recirculating air flow commences and the water cone is chopped off before L_c. By taking for the minimum value of $x_b \approx D_l$, a value found for constant-density jets (Villermaux *et al.* 1994), we get $M_c \approx 35$. An alternative way to determine M_c, which does not require a value for x_b, is to say that the recirculation will start when the local pressure drop caused by the gas turbulence $\frac{1}{2}\rho_g u_g'^2$ is just equal to $\frac{1}{2}\rho_l U_l^2$, which gives a value $M_c = 35$ when taking $u_g' = 0.17U_g$ (Villermaux *et al.* 1994 and Rehab *et al.* 1997).

3.5. *Primary drop formation*

In his review of air-blast atomization, Lefebvre (1980) gives a large number of references which are related to the instability and disruption of gas–liquid interfaces. Most theoretical studies have concentrated on the instability of liquid sheets subjected to a high-velocity gas stream. The resulting drop size in this case is related to the sheet thickness. According to Levebvre, the air–liquid interaction produces unstable waves which break into fragments; these fragments contract into ligaments which in turn break into drops through a Rayleigh-type instability. The problem then is to estimate the size of the ligaments and its dependence on initial conditions. In the coaxial jet configuration, as the water is accelerated by the coflowing air, a large fraction of the liquid mass flux may end up in annular sheets inclined at a angle to the flow which then break in the way described by Levebvre (1980) and Dombrowski & Jones (1963).

When conditions are turbulent–turbulent, the interface velocity has a simple relation with U_g, and from the liquid shedding frequency measurements presented in §3.3, one can evaluate the wavelength of the primary instability, which is just $\lambda_{2D} = U_i/f$. This wavelength is two orders of magnitude larger than the wavelength dominated by surface tension (see Chandrasekhar 1961). The air mixing layer draws out sheets at a certain preferential angle (of the order of 45°) to the jet axis which break into ligaments (see figure 6), possibly in a way similar to the streamwise vortices in a mixing layer or due to an intrinsic instability of the sheet. An order of magnitude estimation of the thickness can be obtained by conservation of mass arguments. The mass flux into a sheet of thickness ξ is $(\xi D_l \pi U_l)$, and on average there are x_b/λ sheets per liquid intact length. A fraction of the total liquid mass is pinched off at the centre (the sheet could also have a helical structure). However, if one assumes that the total mass flow rate of the liquid $\frac{1}{4}\pi D_l^2 U_l$ goes into the sheets, we get

$$\xi = \frac{1}{4}\frac{D_l}{M^{1/2}}\frac{\lambda}{x_b}. \tag{14}$$

Combining (13) and (14) gives $\xi = \lambda/24$. Note that as the sheet is drawn out to larger diameters, D', its thickness decreases (by mass conservation), and it breaks into ligaments. The minimum length of the filaments is $U_i/f = \lambda$, so that $D' \approx D_l + \lambda\cos 45°$. The thickness ξ', and thus the size of the drops formed by Rayleigh instability are then

$$\xi' \approx \xi\frac{D_l}{D'} \approx \frac{D_l}{24(0.7 + D_l/\lambda)}. \tag{15}$$

It should be pointed out that, as it will be shown later, these estimated values are far greater than the drop sizes measured at the jet's centreline, thus indicating that in the interior region of the jet, an additional break-up mechanism must take place.

4. Secondary liquid break-up

The thickness of the viscous liquid layer accelerated by the high-speed annular gas increases with the downstream distance from the nozzle. In addition, the large-scale eddies formed by the merging shear layers developing at the gas/liquid and gas/gas interfaces (see figure 6) entrain lumps of liquid whose size grows as they move downstream. At high liquid/air mass and momentum ratios, these eddies entrain large lumps of liquid, eventually cutting off the central liquid cone (see figures 2*f*, 2*g*, and 2*h*). These liquid lumps are subsequently broken up by the pressure and viscous forces from the mean and turbulent motion of the surrounding turbulent air (secondary atomization). Since the size of the lumps is of the order of the jets' integral length scale, L, they could account for a considerable fraction of the total liquid flow rate, and consequently their secondary atomization could determine the final droplet size distribution in the spray.

After the lumps are pinched off from the liquid cone, the momentum transfer between the air and the liquid results in a complex process involving not only their acceleration, but also their simultaneous break-up and coalescence. To help describe this complex dynamic interaction between the two phases, let us use a single parameter, d (i.e. the diameter of an equivalent spherical liquid droplet of equal volume), to specify the size of each liquid particle present in the jet at a given location $\boldsymbol{x}$, at a given time t. A statistical description of the liquid may then be given by a distribution function (or density function), $f(d, \boldsymbol{x}, \boldsymbol{v}, t)$, defined as the probable number of droplets per unit volume with diameters in the range about d, located in the spatial range about the vector position $\boldsymbol{x}$, with a velocity in the range about $\boldsymbol{v}$, at a time t. An equation describing the time evolution of the distribution function, $f(d, \boldsymbol{x}, \boldsymbol{v}, t)$, may be derived by using arguments similar to those used in the kinetic theory of gases. Following the notation in Williams (1985),

$$\frac{\partial f}{\partial t} = \boldsymbol{\nabla}_x \cdot (\boldsymbol{v} f) - \boldsymbol{\nabla}_v \cdot (\boldsymbol{F} f) + \frac{\partial}{\partial d}(R f) + Q_b' + Q_c' + \Gamma, \tag{16}$$

where $\boldsymbol{F}(d, \boldsymbol{x}, \boldsymbol{v}, t)$ is the force per unit mass on a liquid particle, and $R(d, \boldsymbol{x}, \boldsymbol{v}, t)$ is the time rate of change of its size due to evaporation (which in general also depends on the local temperature and vapour concentration of the surrounding air). The first term on the right-hand side accounts for the changes in f due to the motion of liquid particles in and out of a spatial element $\mathrm{d}\boldsymbol{x}$ by virtue of their velocity $\boldsymbol{v}$, and the second represents the rate of change of the number of particles in the velocity element $\mathrm{d}\boldsymbol{v}$ because of the acceleration $\boldsymbol{f}$. The third term represents the changes in f resulting from liquid evaporation, while Q_b' is the time rate of increase of f due to particle break-up, Q_c' is the rate of change of f due to droplet coalescence, and Γ is the rate of change of f due to collisions (i.e. the changes in f resulting from the variation in the velocity of the particle caused by interparticle collisions which did not result in coalescence). Furthermore, for nearly all vaporization mechanisms, the dependency of R on the droplet size may be expressed approximately by the equation

$$R = -\frac{\chi}{d^k}, \tag{17}$$

where $0 < k < 1$ is independent of d but dependent on the temperature and local vapour concentration of the air surrounding the particle, Williams (1985). In our application, we estimate that the contribution of R to the changes in n becomes vanishingly small at the jet's centreline, since after a short transient length needed to

reach saturation conditions at room temperature, χ becomes very small. (This assumption, and the effect of droplet evaporation will be discussed later in §5.) Thus, neglecting evaporation, the steady-state form of equation (17) becomes

$$\nabla_x \cdot (\boldsymbol{v}f) - \nabla_v \cdot (\boldsymbol{F}f) + Q'_b + Q'_c = 0. \tag{18}$$

Eliminating the velocity dependency by integrating over the whole velocity space, we get

$$\nabla_x \cdot (\bar{\boldsymbol{v}}n) + \int Q'_b \, \mathrm{d}\boldsymbol{v} + \int Q'_c \, \mathrm{d}\boldsymbol{v} = 0, \tag{19}$$

where $n(d, \boldsymbol{x}) = \int f \, \mathrm{d}\boldsymbol{v}$ is the mean number density of droplets of size d at a location $\boldsymbol{x}$, and $\bar{\boldsymbol{v}}(d, \boldsymbol{x}) = (\int \boldsymbol{v}f \, \mathrm{d}\boldsymbol{v}) / \int f \, \mathrm{d}\boldsymbol{v}$ is the mean velocity of the liquid droplet of size d at location $\boldsymbol{x}$. Both of these quantities will be measured experimentally in the present study.

Expanding the first term in equation (19) yields

$$\bar{\boldsymbol{v}} \cdot \nabla_x n = -n \nabla_x \cdot \bar{\boldsymbol{v}} + Q_b + Q_c, \tag{20}$$

where $Q_b = \int Q'_b \, \mathrm{d}\boldsymbol{v}$ and $Q_c = \int Q'_c \, \mathrm{d}\boldsymbol{v}$. Thus, the spatial changes in the mean number density of droplets are due to three mechanisms, namely a convective effect resulting from the motion of particles in and out of a special location $\boldsymbol{x}$ by virtue of their velocity $\bar{\boldsymbol{v}}$, droplet break-up, and droplet coalescence. To close the problem, the mean velocity of the liquid particles $\bar{\boldsymbol{v}}(d, \boldsymbol{x})$ must be calculated from the conservation of mass and linear momentum between the phases, which requires information on $\boldsymbol{F}$. Or as in our case, $\bar{\boldsymbol{v}}(d, \boldsymbol{x})$ will be measured experimentally.

In the following we will analyse, in the context of our specific application, the contributions of each of the three terms in equation (20) to the spatial changes of the mean droplet size distribution, n.

4.1. *Secondary break-up mechanisms*

Following the classical decomposition of the turbulent motion into a mean plus a fluctuating component, we can then classify the forces acting on the liquid particles, τ, as the sum of a force resulting from the relative velocity between the particle and the mean motion of the gas (slip velocity), and a force due to the turbulence of the carrier fluid. To differentiate between the break-up processes resulting from these two effects, we will refer to them as 'shear break-up' and 'turbulent break-up' respectively.

Shear break-up

When a water drop of size d is suddenly exposed to an airflow of relative constant speed $(u_l - u_g)$ break-up will occur if the shear Weber number exceeds a critical value (Hanson *et al.* 1963)

$$We_s = \frac{\rho_l (u_l - u_g)^2 \, d}{\sigma} > (We_s)_c. \tag{21}$$

In our application $(We_s)_c$ does not depend on the viscosity number, N, and approaches a constant value of the order 10 as the droplet diameter decreases. Furthermore, in our high-speed coaxial jets, the droplets are quickly accelerated to velocities equal to, or larger than, that of the carrier fluid (due to the large inertia of the liquid since $\rho_l / \rho_g \gg 1$). Thus, as will be shown from our measurements of u_l and u_g, this Weber number quickly decreases, and this break-up mechanism, although very effective in the near region ($x/D_l \leqslant 7$), becomes inefficient shortly beyond the liquid cone length.

Turbulent break-up

As the liquid becomes accelerated by the high-speed air, the particles remain exposed to the turbulent motion of the surrounding gas, and this may result in further droplet break-up. When the Reynolds number of the air flow is very large, as it is in our application (i.e. of the order of 10^4 to 10^5), Kolmogorov found that if the droplet size compared to the Kolmogorov microscale, η, satisfies

$$d \gg \eta(\nu_l/\nu_g)^{3/4}, \tag{22}$$

the effect of the viscosity inside the drop is unimportant, and the determining factor in the turbulent break-up is only the dynamic pressure caused by the velocity changes over distances of the order of the droplet diameter. The dynamic pressure force from the turbulent motion per unit surface is $\rho_g \overline{u(d)^2}$, where $\overline{u(d)^2}$ is the mean square of the relative velocity fluctuations between two points diametrically opposite on the surface of the droplet. The surface tension force per unit area is σ/d. The turbulent Weber number is then defined as

$$We_t = \frac{\rho_g \overline{u(d)^2}\, d}{\sigma}. \tag{23}$$

Thus, when We_t is greater than a critical value, $(We_t)_c$, of order 1, atomization of the liquid occurs because the dynamic pressure forces from the turbulent motion are sufficiently large to overcome the confinement of the surface tension. To calculate the lower critical Weber number, Taylor (1934) pointed out that the drops are vibrating systems and thus their break-up occurs as the dynamic response to time-dependent pressure fluctuations at a given frequency. Following Taylor's model, Sevik & Park (1973) obtained a general expression for the critical Weber number by setting the characteristic frequency of the turbulent flow equal to the natural frequency of the n-order mode of a spherical droplet undergoing small-amplitude oscillations. They predicted that for $(\rho_l/\rho_g \geqslant 1)$ the lowest critical Weber number (for $n = 2$) is always less than 0.59, decreasing below this value as ρ_l/ρ_g increases. These results are in good agreement with the turbulent critical Weber number of 0.59 quoted by Hinze for Clay's experiments. Note that these critical turbulent Weber numbers, $(We_t)_c$, are considerably smaller than the critical shear Weber number, $(We_s)_c \approx 10$ introduced above. Furthermore, since the air jet is at a very high Reynolds number, at its centreline, an inertial subrange exists in which the energy spectrum of the turbulence conforms to Kolmogorov's hypothesis of local isotropy. In other words, the spectrum of the turbulent velocity fluctuations includes a range of high wavenumbers (the universal equilibrium range) which is uniquely determined by the turbulent dissipation rate in the air. For this local isotropy to exist, the linear scale of the energy-containing eddies must be large compared to the scale of the small energy dissipating eddies. For very small values of $d(d > \eta)$, the form of the universal function can be obtained by dimensional analysis:

$$\overline{u(d)^2} = C(\varepsilon d)^{2/3}. \tag{24}$$

Assuming that the residence time of the liquid in the turbulent region is longer than the break-up time, the maximum stable droplet size, d_{max}, can then be obtained from the relation

$$d_{max} = \left[\frac{\sigma(we_t)_c}{\rho_g}\right]^{3/5} \varepsilon^{-2/5}. \tag{25}$$

At large mean velocities, as is the case in our experiments, the time the drops stay in the fluid, for given constant local turbulent characteristics, may be insufficient for the

breakage process to be terminated and for the liquid to reach a state of equilibrium. Thus, equation (25) is a necessary but not a sufficient condition. We will return to this point below.

Since $(\overline{u(d)^2})^{1/2}$ is only a statistical value of the velocity difference at a distance d, it is possible however rare, that much greater velocity differences could appear at the same distance d. Furthermore, this classical, inertial subrange theory could be modified by including the effect of intermittency in the turbulent field, Baldyga & Bourne (1993).

The time evolution of the distribution function can then be calculated by incorporating breakage relationships (Konno *et al.* 1980)

$$Q_b = \int_d^\infty m(d')\,\gamma(d', d)\,K_b(d')\,n(d')\,\mathrm{d}(d') - K_b(d)\,n(d), \tag{26}$$

where K_b is the break-up frequency of drops of size d, $m(d')$ is the mean number of daughter drops formed through the break-up, and $\gamma(d, d')$ is the distribution of daughter drops formed through the break-up of a parent drop of size d'.

4.2. *Droplet coalescence*

The local turbulent velocity fluctuations also result in collisions between droplets, and thereby the chance of coalescence. However, it is well known that only a fraction of those collisions will result in coalescence. When two droplets collide, a thin film of air forms between the two colliding droplets and acts as a cushion which may cause them to rebound. If the time involved in a collisions is sufficiently large for the air film separating the droplets to gradually thin to below a certain threshold, the boundary between the two droplets will adhere and their coalescence will occur. Inversely, if the agitation of the medium is sufficiently high (large ϵ) the time involved in the collision will be shorter than that needed for the film's drainage, and the droplets will rebound without undergoing coalescence. The collision residence time which leads to an adhesion will obviously depend on the size of the droplets, on the properties of the dispersed and continuous media, and on the intensity of the turbulence in both media. The frequency of coalescence can then be calculated as a product of the collision frequency and a coalescence efficiency which depends on the ratio between the droplet's contact time, $\bar{t}$, and a critical drainage time, $\bar{T}$. The latter can be readily estimated by computing the time needed to bring together two droplets of size d. The force needed to bring together two circular plates of diameter d (an approximation to the pancake shape of two droplets at the point of impact) separated by a distance h_0 is $F = 3\pi\mu_g\,u(d/2)^2/2h_0^3$ (see e.g. Landau & Lifshitz 1989). Since the relative inertia is $\rho_l(\varepsilon d)^{2/3}\,d^2$ the drainage time is $\bar{T} \approx (\mu_g/\rho_l)\,\varepsilon^{-2/3}\,d^{-2/3}$ (see also Tsouris & Tavlarides 1988, and Jeffreys & Davies 1971). The contact time can be estimated as the reciprocal of the fluid velocity fluctuations between two points separated by a distance equal to the droplet's diameter, or turnover time $\bar{t} \approx \varepsilon^{-1/3}\,d^{2/3}$. The coalescence efficiency is then

$$\prod \approx \exp(-\bar{T}/\bar{t}). \tag{27}$$

The maximum drop diameter for which separation is possible (coagulation will be prevented) is given by the cut-off condition $\bar{t} = \bar{T}$ which gives

$$d_{max} \approx \frac{\mu_g}{\rho_l}\varepsilon^{-1/4}. \tag{28}$$

The above argument is equivalent to postulating that the adhesion of two droplets of size d will take place if the kinetic energy E_k of the two droplets relative to each other

is less than a critical energy of adhesion E_a (Shinnar 1961). If the two droplets are of equal diameter and the thickness of the air film h_0 separating them is much greater than d, the energy of adhesion is $E_a = A(h_0)\,d$, and the kinetic energy of their relative motion is $E_k = \rho_l \overline{u(d)^2}\, d^3$, where A and h_0 are independent of d. Thus, the maximum drop diameter for which separation is possible (coagulation will be prevented) is given by

$$\frac{\rho_l\, d_{max}^{8/3}\, \varepsilon^{2/3}}{A(h_0)} = \text{const.}, \tag{29}$$

resulting in

$$d_{max} \approx \left[\frac{A(h_0)}{\rho_l}\right]^{3/8} \varepsilon^{-1/4}, \tag{30}$$

which gives the same dependency on ε as shown in equation (28).

The time evolution of the droplet distribution function due to coalescence can then be calculated as the product of a collision frequency and a coalescence efficiency, Π (see for example Bapat 1982; Ramakrishna 1985; Tsouris & Tavlarides 1994).

5. Experimental evidence on the far-field droplet size

Measurements of the radial variation of the mean droplet diameter show that the mean size of the droplets is minimum at the jet's centreline, and it increases as one moves toward the outer edges of the jet (figure 7). This behaviour was consistently observed for all the measurements performed at downstream distances greater than 10 jet diameters. Since the primary breakup mechanism described in §3 is much more efficient at the edge of the jet (since the shear is maximum at the gas–liquid interface) these measurements indicate that after the liquid is broken by the primary shear instability, further break-up (of the type described in §4) must take place downstream of the liquid cone and is more effective at the jet's centre than at its edges.

5.1. *Dependence of the droplet diameters on the water and air flow rates*

To investigate the effect of the water flow rate on the atomization process, we conducted a series of measurements at constant gas velocity U_g while varying the water velocity U_l. In figure 8 the variation of the mean droplet size, D_{32}, with the downstream distance along the jet's centreline is plotted for various water velocities ranging from 0.13 to 0.55 m s^{-1}. The important points to be noted from these measurements are the following. (*a*) The droplet diameter does not decrease to an asymptotic value at large downstream distances from the nozzle, but rather it shows a non-monotonic dependence on x/D_g. The mean diameter was always found first to decrease, reaching a minimum, and then to increase monotonically with the downstream distance. (*b*) The value of the minimum mean droplet diameter increases with the water flow rate (increasing U_l). (*c*) The downstream location, x/D_g, of this minimum increases with U_l. (*d*) After reaching a minimum, the mean droplet size follows a nearly linear dependence on the downstream distance with a slope independent of U_l.

The effect of the air flow rate on the liquid atomization was also investigated by fixing the water velocity, U_l, while varying the air velocity, U_g. Figure 9 shows the variation of the mean diameter D_{32}, with a downstream distance for four different representative air flow rates. Similarly to figure 8, the evolution of the mean droplet diameter always shows a non-monotonic dependence on x/D_g, first decreasing and then increasing. It should be noted that the value of the minimum droplet diameter

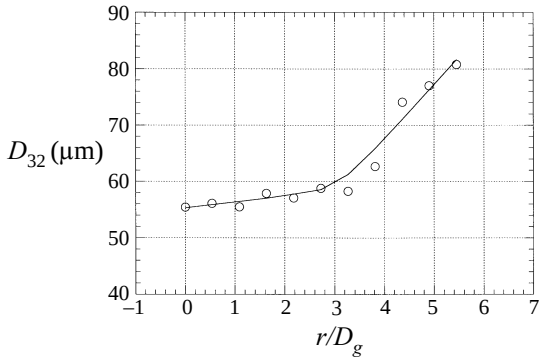

FIGURE 7. Radial variation of the Sauter mean diameter (D_{32}) at 30 diameters downstream of the nozzle's exit. At the outer edges of the jet ($r/D_g > 3$) the droplet size increases to up to 50 % above the centreline value. $U_l = 0.23$ m s^{-1}, $U_g = 126$ m s^{-1}.

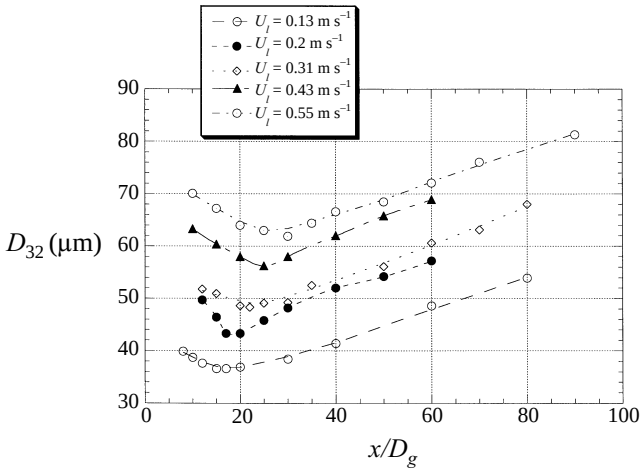

FIGURE 8. Downstream variation of the Sauter mean diameter (D_{32}) measured at the jet's centreline, $U_g = 140$ m s^{-1} and $U_l = 0.13$, 0.20, 0.31, 0.43 and 0.55 m s^{-1}.

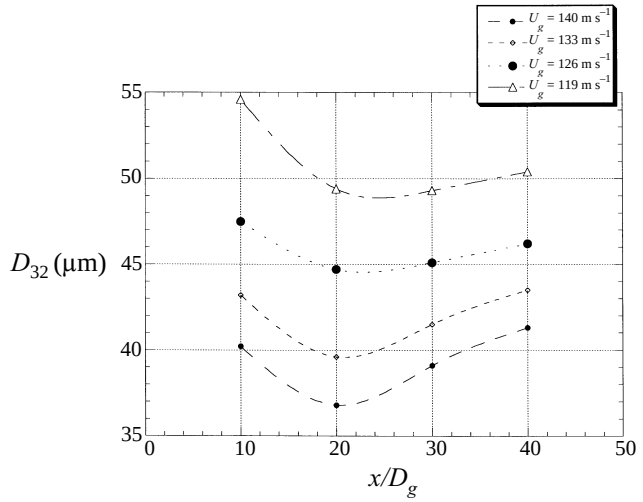

FIGURE 9. Downstream variation of the Sauter mean diameter (D_{32}) measured at the jet's centreline. $U_l = 0.13$ m s^{-1}, and $U_g = 119$, 126, 133 and 140 m s^{-1}.

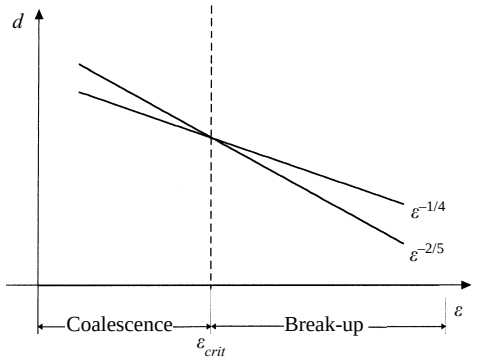

FIGURE 10. Equilibrium maximum droplet diameter d as a function of the dissipation rate of turbulent kinetic energy of the air. Note that for $\varepsilon < \varepsilon_{crit}$ the maximum diameter is determined by coalescence while in regions where $\varepsilon > \varepsilon_{crit}$ it is determined by breakup.

decreases with the air flow rate (increasing U_g), while the location of the minimum decreases with U_g. After the minimum, the mean drop size also increases linearly with x/D_g.

The existence of two regions of the spray in which the mean droplet diameter exhibits well-differentiated behaviour is evidence of the competing contributions of the different terms in equation (20) to the changes in the steady-state value of the droplet distribution function $n(d, \boldsymbol{x})$.

To illustrate the nature of these two regions, let us for the moment ignore the possible contributions of $n\boldsymbol{\nabla}_x \cdot \bar{\boldsymbol{v}}$ to the changes in n, and assume that the evolution of the size distribution of droplets depends only on the simultaneous occurrence of break-up and coalescence, Q_b and Q_c (we will discuss the effect of the acceleration term later). Then,

$$\bar{\boldsymbol{v}} \cdot \boldsymbol{\nabla}_x n = Q_b + Q_c. \tag{31}$$

Owing to the large Re of our experiments, the jet's turbulence closely satisfies the conditions of local isotropy at its centreline. Thus, to a first approximation, assuming that the droplets stay long enough in a region of sufficiently large turbulent kinetic energy, the maximum droplet size that will withstand break-up is $d_{max} \approx \varepsilon^{-2/5}$ (equation (25)). Similarly, the droplet size above which coalescence will be unlikely to occur is $d_{max} \approx \varepsilon^{-1/4}$ (equation (30)). Since both the break-up and coalescence processes are determined only by the dissipation rate of the turbulent kinetic energy, ε, through different power exponents, it easily follows that depending on the local value of ε, one process will dominate the other. As the energy dissipation decreases downstream, in the region of high values of ε (near field, small x/D) break-up is dominant and the droplet size is determined by equation (25), while in regions of small dissipation (far field, large x/D_g) it will be controlled by the coalescence process, and the size is given by equation (30) (Shinnar 1961) (see figure 10). In the following we will refer to each of these regions as the break-up region (descending portion in figures 8 and 9), and the coalescence region (ascending portion in figures 8 and 9).

The droplet break-up region

As discussed above in relation to the radial measurements shown in figure 7, the lumps of liquid pinched off from the central liquid cone must undergo secondary break-up by the turbulent fluctuations of the continuous phase. As shown above, if the residence time of the liquid in the highly dissipative region of the turbulent jet is long

enough for the break-up to be completed, a local equilibrium will always be reached. Thus, one will conclude that, since ε is maximum near the end of the potential core, the minimum in figures 8 and 9 should always be at a location $x/D_g \approx 5$–8 (increasing as the air/water momentum ratio decreases). However, as is apparent from the above experimental results, this is never the case; and the minimum always occurs at distances $x/D_g \approx 15$–20, much further downstream from the nozzle. From this fact alone, it is obvious that although the dissipation rate is higher near the nozzle's exit, the liquid residence time is shorter than that needed for break-up. Equilibrium will then be reached at a critical distance downstream from the nozzle, x_{crit}, where the break-up time of the droplet equals its residence time. Assuming that the droplet break-up time is of the order of the eddy turnover time $t_b = d_{max}/(\overline{u(d)^2})^{1/2}$, introducing equation (24), we get

$$t_b \approx \varepsilon^{-1/3} d_{max}^{2/3}. \tag{32}$$

On the other hand, the liquid residence time can be estimated as

$$t_r = \int^x \frac{\mathrm{d}\xi}{U(\xi)}, \tag{33}$$

where $U(\xi)$ is the mean velocity of the liquid drops along the jet's centreline. Since $U(\xi)$ is of the order of the mean velocity of the jet along its centreline, it is reasonable to assume that $U(\xi) \approx U_g/x^\beta$ with β being a constant of order 1 which depends on the water to air mass flow rate ($\beta = 1$ if $m = 0$). Integrating equation (33), we get

$$t_r \approx \frac{x^{(\beta+1)}}{(\beta+1)\, U_g}. \tag{34}$$

Combining (32) and (33), the critical equilibrium length can then be estimated as

$$x_{crit} \approx U_\gamma^{-(\beta+1)}\, \varepsilon^{-1/3(\beta+1)}\, d_{max}^{2/3(\beta+1)}, \tag{35}$$

and introducing equation (25), we get

$$x_{crit} \approx U_g^{1/(\beta+1)}\, \varepsilon^{-3/5(\beta+1)}\, (\sigma/\rho_g)^{2/5(\beta+1)}. \tag{36}$$

What remains now is to estimate the turbulent dissipation rate along the jet's centreline. It is well known that in a single-phase jet, the dissipation rate is proportional to the initial kinetic energy of the jet per unit mass per unit time, U_0^3/D_g, where U_0 is the initial jet velocity and D_g is the diameter of the nozzle. It is then reasonable to postulate that in our two-phase flow case, the dissipation rate in the gas should now be proportional to the total initial flux of kinetic energy (contained mainly in the gas) per unit total mass (gas plus liquid). Thus,

$$\varepsilon \approx \frac{U_g^3}{(1+\rho_l\, U_l/(\rho_g\, U_g))^\omega\, D_g}, \tag{37}$$

where ω depends on the liquid to air mass flow rate, m, and will be determined experimentally. Combining equations (36) and (37), and taking $\beta = 0$†, we get

$$x_{crit} = U_g^{-4/5} \left[\frac{1}{(1+\rho_l\, U_l/(\rho_g\, U_g)^\omega\, D_g}\right]^{-3/5} \left(\frac{\sigma}{\rho_g}\right)^{2/5}. \tag{38}$$

† In our two-phase flow jet, the mean centreline velocity is approximately constant for the first five to eight diameters, at which point our measurements show a decrease $U(x) \approx U_g/x^\beta$, with $0.2 \leqslant \beta \leqslant 0.6$, and the value of β increasing with M. Thus, as a conservative estimate, we take $\beta = 0$.

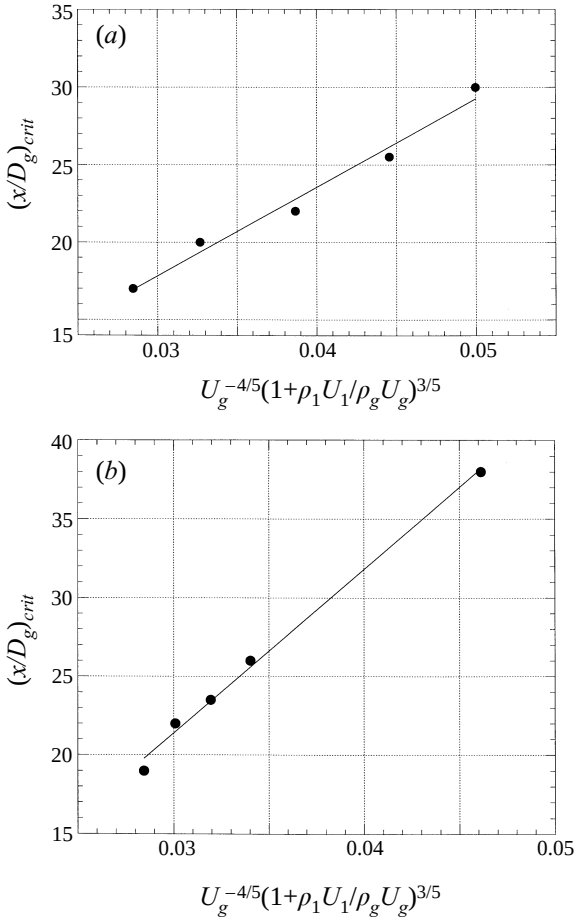

FIGURE 11. (*a*) Comparison of the measured downstream location of the droplet break-up equilibrium point x_{crit} in figure 8 with the prediction given by equation (38) (solid line). (*b*) Comparison of the measured downstream location of the droplet break-up equilibrium point x_{crit} in figure 9 with the prediction given by equation (38) (solid line).

Equation (38) shows a dependence of x_{crit} on U_l and U_g consistent with that observed experimentally, i.e. the downstream location of the minimum (i.e. the location at which equilibrium is reached, $x = x_{crit}$) increases with U_l while it decreases with U_g. Figure 11(*a*, *b*) shows the measured values of x_{crit} for all the U_l and U_g corresponding to figures 8 and 9. Observe that the dependence predicted by equation (38) is consistent with the experimental results. Furthermore, using (38) as a correlation of the experimental data, we can estimate ω to be approximately equal to 1.

The value of the mean diameter at the equilibrium (minimum in figures 8 and 9) is then calculated by combining equations (25) and (37) to give

$$d_{max} \approx \left[\frac{\sigma}{(We_t)_c}\right]^{3/5}\left[\frac{U_g^3}{(1+\rho_l U_l(\rho_g U_g)^{\omega} D_g}\right]^{-2/5}. \tag{39}$$

Since the drop size predicted by the secondary atomization argument is the maximum drop size, we have selected the D_{90} (the diameter for which 90% of the total liquid volume is in droplets of smaller diameters) as the relevant parameter to measure. The

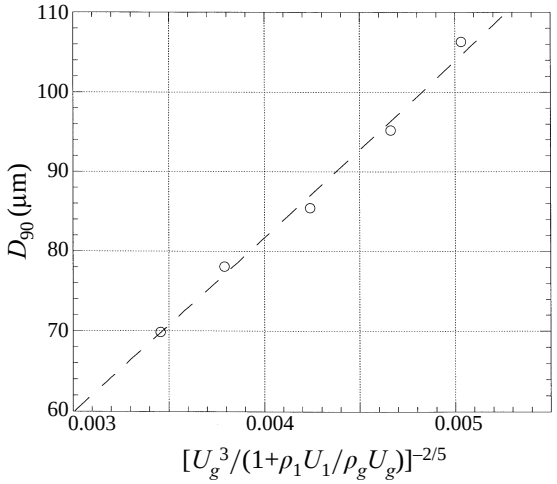

FIGURE 12. Dependence of the measured maximum droplet diameter at the equilibrium point (D_{90}) on the flux of total kinetic energy of the air jet per unit total mass of the system. $U_g = 140$ m s^{-1} and $U_l = 0.13$, 0.20, 0.31, 0.43 and 0.55 m s^{-1}.

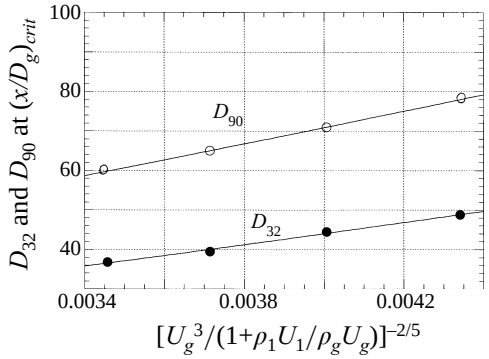

FIGURE 13. Dependence of the measured maximum droplet diameter at the equilibrium point (D_{90}) on the flux of total kinetic energy of the air jet per unit total mass of the system. $U_l = 0.13$ m s^{-1}, and $U_g = 119$, 126, 133 and 140 m s^{-1}.

dependence of D_{90} measured at the minimum on U_l and U_g is shown in figures 12 and 13. Note that, consistent with the predicted dependence given above, in both cases D_{90} is found to correlate well with $[U_g^3/(1+\rho_l U_l/(\rho_g U_g))]^{-2/5}$ where ω in equation (38) is also found to be 1.

The droplet coalescence region

Downstream of x_{crit} the turbulent kinetic energy of the air can no longer provide sufficient pressure deformation forces to overcome the confinement by the surface tension. From this location onward, droplet coalescence, acceleration, and evaporation (although, as discussed before, negligible in our case) will determine the mean drop size.

In the coalescence region, located downstream of the minimum in figures 8 and 9, the most probable drop size above which coalescence will be prevented by the turbulence is given by equation (30). Introducing the value of the estimated turbulent dissipation rate, and assuming that in the far field of the jet decays as $(x/D_g)^{-4}$ similarly

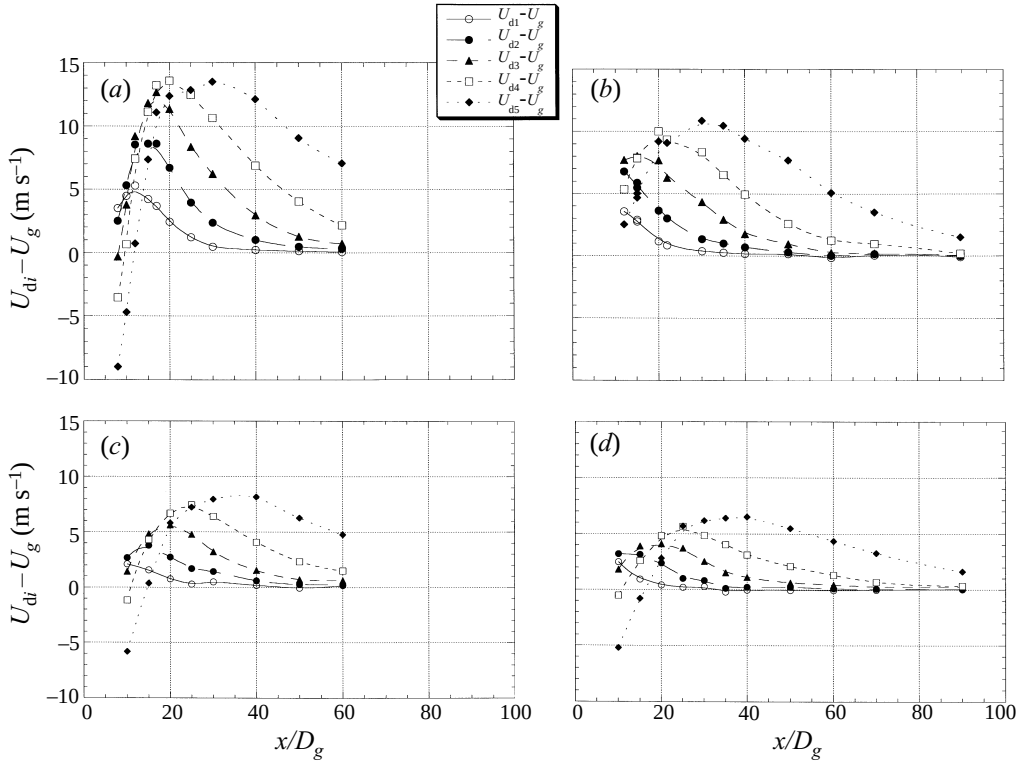

FIGURE 14. Mean slip velocity between the droplets and the surrounding air measured at the jet's centreline. The droplet sizes have been classified in six size bins: D_1 for sizes between 5 and 18 μm; D_2 for sizes between 18 and 36 μm, D_3 for sizes between 36 and 75 μm, D_4 for sizes between 75 and 110 μm, and D_5 for droplets greater than 110 μm. The gas has been measured by the droplets in the size bin with droplets smaller than 5 μm. (*a*) $U_g = 140$ m s^{-1} and $U_l = 0.2$ m s^{-1}, (*b*) $U_g = 140$ m s^{-1} and $U_l = 0.31$ m s^{-1}, (*c*) $U_g = 140$ m s^{-1} and $U_l = 0.41$ m s^{-1}, (*d*) $U_g = 140$ m s^{-1} and $U_l = 0.53$ m s^{-1}.

to the decay observed in one-phase jets, Friehe, Van Atta & Gibson (1977) (an assumption which will lose validity for very large M) we get

$$(d_{max})_{coalescence} \approx \left[\frac{U_g^3}{(1+\rho_l U_l/(\rho_g U_g))^{\alpha} D_g}\right]^{-1/4}\left(\frac{x}{D_g}\right), \tag{40}$$

which shows that in the coalescence region the droplet diameter grows linearly with the downstream distance, in agreement with the measured evolution given in figures 8 and 9. Note also that the local coalescence equilibrium assumption made above gives a dependence of the slope on U_l and U_g. However, this dependence is not apparent in the experimentally observed evolution (figures 8 and 9), where it appears that the slopes are independent of U_l and U_g.

5.2. *Effect of the droplet acceleration*

Let us now turn our attention to the analysis of the possible contribution of $-n\boldsymbol{\nabla}_x \cdot \bar{\boldsymbol{v}}$ to the downstream variation of n. To estimate the acceleration of the droplets $\boldsymbol{\nabla}_x \cdot \bar{\boldsymbol{v}}$ let us consider one droplet in isolation. To a first approximation, the droplet inertia is balanced by the viscous drag

$$\bar{\boldsymbol{v}}\frac{\mathrm{d}\bar{\boldsymbol{v}}}{\mathrm{d}x} \approx \frac{\mu_2(\bar{\boldsymbol{v}} - U_g)}{\rho_1 d^2}, \tag{41}$$

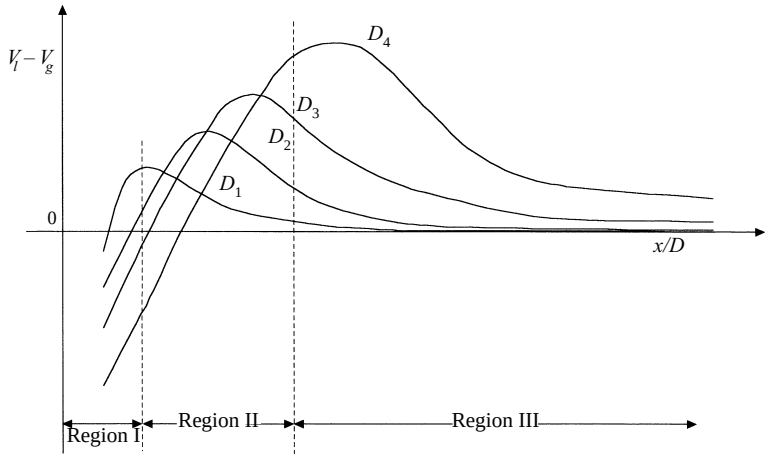

FIGURE 15. Region I – liquid acceleration; Region II – acceleration of large size droplets coexisting with deceleration of small ones; Region II – droplet deceleration.

where, for simplicity, we have assumed Stokes' drag law, and neglected unsteady terms such as added mass, Basset, and effects. The droplet acceleration is inversely proportional to the square of its diameter, and the relaxation length for the droplet to be accelerated to the gas velocity, U_g, is then

$$x_{accel} \approx \frac{\rho_l U_g d^2}{\mu_g}. \tag{42}$$

Figure 14 shows the measured values of $\bar{v}$ for four representative cases. These measurements were obtained by discretizing the droplet distribution function into six droplet sizes bins, with the one corresponding to $d < 3$ μm used to measure the gas velocity. Note that as one would expect, the downstream evolution of the mean droplet velocities is made up of three regions (see figure 15).

Region I. In the near field, all the droplets regardless of their size are moving at velocities lower than that of the gas, and are being accelerated (positive acceleration) by the viscous and pressure forces $\boldsymbol{F}$. Since for each drop, its relaxation length is proportional to d^2, the smaller droplets will begin to move faster than the larger ones. Therefore, since assuming the absence of break-up or coalescence $\bar{v} \cdot \nabla_x n = -n \nabla_x \cdot \bar{v}$, it follows that the effect of the initial acceleration in the near field is to increase the mean droplet size (observe that the smaller droplets move faster than the larger ones, and the mean size increases). Since this result is in direct opposition to the experimentally observed decay in the size, it can be considered as a corroboration of the assumption made above that the size decay in the first region in figures 8 and 9 is determined by break-up and not by acceleration effects.

Region II. After the droplets are accelerated to the gas velocity, their inertia leads to a velocity overshooting region whereby the larger droplets pass the gas while the smaller ones quickly begin to relax again to reach the gas velocity. Thus, in this second region, the term $\nabla_x \cdot \bar{v}$ will lead to a decrease in the mean droplet size. The extent of this second region can be estimated by introducing equations (25) and (37) into (42) to give

$$x_{accel} \approx \frac{\rho_l U_l}{\mu_g} \left[\frac{\sigma}{(We_l)_c} \right]^{6/5} \left[\frac{U_g^3}{(1 + \rho_l U_l / (\rho_g U_g))^m D_g} \right]^{-4/5}, \tag{43}$$

a result again consistent with the experimentally observed dependencies of the air and water velocities.

Region III. After the maximum drop size has reached a maximum velocity, all droplets regardless of their size will decelerate leading to an increase in the mean droplet size. (Note that $\nabla_x \cdot \bar{v}$ is always negative and larger for the smaller droplets.) Thus, the effect of the droplet acceleration leads to the same dependence of the mean size as did the coalescence effects. However, since the magnitude of $\nabla_x \cdot \bar{v}$ is very small, this contribution is most likely small compared to the coalescence effects.

5.3. *Effect of the turbulent dispersion and droplet evaporation*

Implicit in our discussion of equation (20), and in particular in the analysis of the terms $\bar{v} \cdot \nabla_x n$ and $n \nabla_x \cdot \bar{v}$ in the preceding section, was that the spray behaves as a quasi-one-dimensional flow, i.e. we accounted only for the transport effects resulting from the axial motion of the spray. However, as was shown in figures 2, 3 and 6, the lateral spreading of the jet is dominated by the presence of a large-scale coherent eddy structure. These eddies are known to dominate the turbulent diffusion of the droplet across the spray, whereby the droplets are dispersed laterally, according to their size (Lazaro & Lasheras 1992*a*, *b*; Longmire & Eaton 1992, and Kiger & Lasheras 1995).

This large-scale lateral transport results in two main effects. The first one is to produce a downstream increase in the mean droplet size. Recall from figure 7 that, near the nozzle, the mean droplet size is considerably larger at the edges of the spray than on its centreline. As one moves downstream, these large coherent eddies, with scales comparable to the radial thickness of the spray, will ultimately tend to homogenize the mean size of the droplets across the spray. This is an effect consistent with our measurements of the salter mean diameter, which shows that as one moves downstream distances larger than 80 to 100 nozzle diameters, the mean size of the droplets becomes uniform across the spray.

The second effect of the large-scale eddies is to entrain ambient air into the spray across distances comparable to the spray's radius. Since the entrained air is not saturated with water vapour, this will contribute to some evaporation of the water droplets. Thus, at some distance downstream from the nozzle, our assumption of negligible evaporation effects will break down, and the term involving R in equation (16) should be retained in the analysis. However, notice that the evaporation effects will contribute in the opposite way to the measured increase of the mean diameter with downstream distance (figures 8 and 9), indicating that the assumption of negligible evaporation is most likely a reasonable one.

6. Conclusions

The atomization of a liquid jet by a high-momentum turbulent annular jet has been shown to be the result of a dual process. In the near field, the break-up process is dominated by the shedding of liquid sheets or ligaments. In the far field, a secondary breakup process may also take place whereby liquid lumps pinched off from the jet are split by the turbulent stresses of the air jets. The measurements of the shedding frequency in the near field are shown to be qualitatively described by the simple phenomenological model. For initially laminar water jets, it was found that this frequency increases proportionally to the square of the gas velocity. However, in the case of an initially turbulent water jet, it was found to exhibit a linear increase with the air velocity. An entrainment model was developed to predict qualitatively the liquid intact length. It was shown that in the case of large initial aerodynamic Weber numbers

and high gas Reynolds numbers, the liquid intact length depends mainly on the air to water momentum ratio. This result underscores the relevance of the momentum ratio to the breakup process in this type of air blast atomizer.

The far field of the spray jet was found to be characterized by two well-defined regions: an initial region where the mean droplet size measured at the jet's centreline monotonically decreases with the downstream distance, followed by a second region where the droplet's diameter increases with the downstream distance. The role of the secondary droplet break-up in the size distribution measured in these regions was also investigated, and an attempt was made to use the classical concepts of local isotropy, first proposed by Kolmogorov, to qualitatively explain the observed downstream variation of the droplet's size and its dependence on the water and air velocities.

Simplified models of the effect of the turbulent energy dissipation in the gas on the break-up and coalescence of the droplets were developed and compared to the experimental evidence resulting in good, qualitative agreement. The first region was shown to be dominated by the secondary break-up process. Both the values of the minimum droplet size (reached at the equilibrium point), and the downstream location of this equilibrium point were found to be well predicted by the model. The location of the minimum droplet size was found to decrease with the gas's velocity, while it increased with the liquid's velocity. Correlations of the droplet size measurements made based on the local isotropy model indicate that the dissipation rate of the turbulence in the air jet is approximately proportional to the total kinetic energy flux (primarily contained in the air jet) per unit total mass (air + water). The increase in the droplet size observed in the second region was found to be the result of droplet coalescence and droplet deceleration, with the latter playing a minor role. A simple coalescence efficiency model based on the dissipation rate appears to be in good qualitative agreement with the observed increase of the mean droplet diameter with downstream distance, and the dependence of the mean droplet diameter on water and liquid velocity.

Support for this work was provided by grants from United Technologies Corporation and the Societe Europeenne de Propulsion. The authors are grateful for assistance provided by Professor Kenneth Kiger, Ms Monica Orski, and Mr Carlos Martinez in various stages of the experimentation. Valuable discussions with Dr Christophe Clanet are also greatly appreciated.

REFERENCES

Adelberg, M. 1968 Mean drop size resulting from the injection of a liquid jet into a high-speed gas stream. *AIAA J.* **6**, 1143–1147.

Baldyga, J. & Bourne, J. 1993 Drop break-up and intermittent turbulence. *J. Chem. Engng Japan* **26**, 738–741.

Bapat, P. M. 1982 Mass transfer in liquid–liquid continuous flow stirred tank reactor. PhD dissertation. Illinois Institute of Technology, Chicago.

Burick, R. J. 1972 Space storable propellant performance program. Coaxial injectors characterization. *NASA CR*-120936.

Chandrasekhar, S. 1961 *Hydrodynamic and Hydromagnetic Stability*. Dover.

Clay, P. H. 1940 Splitting in dispersion processes. *Proc. R. Acad Sci. Amsterdam* **43**, 852–858.

Dimotakis, P. E. 1986 Two-dimensional shear layer entrainment. *AIAA J.* **24**, 1791–1796.

Dombrowski, N. & Johns, W. R. 1963 The aerodynamic instability and disintegration of viscous liquid sheets. *Chem. Engng Sci.* **18**, 203–214.

Engelbert, C., Hardalupas, Y. & Whitelaw, J. H. 1995 Breakup phenomena in coaxial airblast atomizers. *Proc. R. Soc. Lond.* A **451**, 189–229.

Eroglu, H., Chigier, N. & Farago, Z. 1991 Coaxial atomiser liquid intact lengths. *Phys. Fluids* A **3**, 303–308.

Farrago, Z. & Chigier, N. 1992 Morphological classification of disintegration of round jets in a coaxial airstream. *Atomization and Sprays* **2**, 137–153.

Friehe, C. A., Van Atta, C. W. & Gibson, C. H. 1972 Jet turbulence: dissipation rate measurements and correlations. In *Proc. AGARD Conf. on Turbulent Shear Flows, London September 1971. AGARD CP* 93, 1972.

Gomi, H. 1985 Pneumatic atomization with coaxial injectors. *NAL-TR*-888T, N 86-27595.

Hanson, A. R., Domich, E. G. & Adam, H. S. 1963 Shock tube investigation of the break-up of drops by air blast. *Phys Fluids* **6**, 1070–1080.

Hardalupas, Y. & Whitelaw, J. H. 1994 The characteristics of sprays produced by coaxial airblast atomizers. *J. Propulsion Power* **10**, 453–460.

Hinze, J. O. 1955 Fundamentals of the hydrodynamic mechanism of splitting in dispersion processes. *AIChE J.* **1**, 289–295.

Hopfinger, E. & Lasheras, J. C. 1994 Break-up of a water jet in a high velocity coflowing air. In *Proc. Sixth Intl Conf. on Liquid Atomization and Spray Systems* (ed. A. J. Yule & C. Dumouche), pp. 110–117. Begell House.

Hoyt, J. W. & Taylor, J. J. 1977 Waves on water jets. *J. Fluid Mech.* **83**, 119–127.

Ingebo, R. D. 1992 Effect of gas mass flux on cryogenic liquid break-up. *Cryogenics* **32**, 191–193.

Jeffreys, G. V. & Davies, G. A. 1971 Coalescence of liquid droplets and liquid dispersion. In *Recent Advances in Liquid–Liquid Extraction* (ed. C. Hanson), p. 495. Pergamon.

Keller, F. X., Li, J., Vallet, A., Vandromme, D. & Zaleski, S. 1994 Direct numerical simulation of interface breakup and atomization. In *Proc. Sixth Intl Conf. on Liquid Atomization and Spray Systems* (ed. A. J. Yule & C. Dumouche). Begell House.

Kiger, K. & Lasheras, J. C. 1995 Effect of vortex pairing on particle dispersion and kinetic energy transfer in two-phase turbulent shear layers. *J. Fluid Mech.* **303**, 149–165.

Kolmogorov, A. N. 1949 On the disintegration of drops by turbulent flows. *Dokl. Akad. Nauk. SSSR* **66**, 825–828.

Lane, W. R. 1951 Shatter of drops in stream of air. *Ind. Engng Chem.* **43**, 1312–1317.

Landau, L. D. & Lifshitz, E. M. 1959 *Course of Theoretical Physics, Vol. 6. Fluid Mechanics*. Pergamon.

Lazaro, B. J. & Lasheras, J. C. 1992*a* Particle dispersion in the developing free shear layer. Part 1. The unforced flow. *J. Fluid Mech.* **235**, 143–178.

Lazaro, B. J. & Lasheras, J. C. 1992*b* Particle dispersion in the developing free shear layer. Part 2. The forced flow. *J. Fluid Mech.* **235**, 179–221.

Lefebvre, A. H. 1989 *Atomization and Sprays*. Hemisphere.

Longmire, E. & Eaton, J. 1992 Structure of a particle laden round jet. *J. Fluid Mech.* **236**, 217–257.

Mayer, W. O. H. 1993 Zur koaxialen flussgkeitszerstanburg im hinblick auf die treibstoff-aufbereitung in raketen-triebwerken. *DLR-FB* 93-09. Germany.

Nukiyama, G. E. & Takasawa, Y. 1939 Experiments on the atomization of liquids by means of air streams, parts III and IV. *Trans. Soc. Mech. Engrs Japan* **5** (18), 63–75.

Pilch, M. & Erdman, C. A. 1987 Use of breakup time and velocity history data to predict the maximum size of stable fragments for acceleration induced breakup of a liquid drop. *Intl J. Multiphase Flows* **13**, 741–757.

Rayleigh, Lord 1878 On the instabilities of jets. *Proc. Lond. Math. Soc.* **10**, 4–13.

Raynald, L. 1997 Instabilité et entrainement à l'interface d'une couche de mélange liquide-gaz. PhD thesis, Institute National Polytechnique de Grenoble, France.

Raynald, L., Villermaux, E., Lasheras, J. C. & Hopfinger, E. J. 1997 Primary instability in liquid–gas shear layers. In *Proc. Symp. on Turbulent Shear Flows 11*, Vol. 3, pp. 1–5.

Raynald, L., Villermaux, E. & Hopfinger, E. J. 1988 Primary instability of a plane liquid–gas shear layer. *J. Fluid Mech.* (submitted).

Ramakrishna, D. 1985 The status of population balances. *Rev. Chem. Engng* **3**, 49.

Rehab, H., Villermaux, E. & Hopfinger, E. J. 1997 Flow regimes of large-velocity-ratio coaxial jets. *J. Fluid Mech.* **345**, 357–381.

Rizkalla, A. A. & Lefebvre, A. H. 1975 The influence of air and liquid properties on air blast atomisation. *Trans. ASME*, 316–320.

Schlichting, H. 1987 *Boundary Layer Theory*, 7th Edn. McGraw-Hill.

Sevik, M. & Park, S. H. 1973 The splitting of drops and bubbles by turbulent fluid flows. *J. Trans. ASME Fluids Engng* **95**, 53–60.

Shinnar, R. 1961 On the behaviour of liquid dispersions in mixing vessels. *J. Fluid Mech.* **10**, 259–275.

Sutton, G. P. 1992 *Rocket Propulsion Elements*. Wiley and Sons.

Taylor, G. I. 1934 The formation of emulsion in definable field of flow. *Proc. R. Soc. Lond.* A **146**, 501.

Tsouris, C. & Tavlarides, L. L. 1994 Breakage and coalescence models for drops in turbulent dispersions. *AIChE J.* **40**, 395–406.

Villermaux, E. 1995 Fast bimolecular reactions in high Reynolds number turbulence: structure of the reactive interface and surface of reaction. In *Advances in Turbulence V* (ed. R. Benzi), pp. 529–533. Kluwer.

Villermaux, E. & Hopfinger, E. J. 1994*a* Periodically arranged co-flowing jets. *J. Fluid Mech.* **263**, 63–92.

Villermaux, E. & Hopfinger, E. J. 1994*b* Self-sustained oscillations of a confined jet: a case study for the non-linear delayed saturation model. *Physica* D **72**, 230–243.

Villermaux, E., Rehab, H. & Hopfinger, E. J. 1994 Breakup régimes and self-sustained oscillations in coaxial jets. *Meccanica* **29**, 393–401.

Weber, C. 1931 Zum zerfall eines flussigkeitstrahles (on the disruption of liquid jets). *Z. Angew. Math. Mech.*, vol. II, no. 2.

Wierzba, A. & Takayama, K. 1987 Experimental investigations of liquid droplet breakup in a gas stream. *Rep. Inst. High Speed Mech.* **53** (382) 2–93.

Williams, F. A. 1985 *Combustion Theory*, 2nd Edn. The Benjamin/Cummings Publishing Company.

Zaleski, S., Jie Li, & Succi, S. 1995 Two-dimensional Navier–Stokes simulation of deformation and breakup of liquid patches. *Phys. Rev. Lett.* **75**, 244–247.